Editors' Suggestion

Elastic scattering and rotational excitation of H_2 by electron impact: Convergent close-coupling calculations

Liam H. Scarlett,[1,*] Una S. Rehill,[1] Mark C. Zammit,[2] Nicolas A. Mori,[1] Igor Bray,[1] and Dmitry V. Fursa[1]

[1]*Curtin Institute for Computation and Department of Physics and Astronomy, Curtin University, Perth, Western Australia 6102, Australia*

[2]*Theoretical Division, Los Alamos National Laboratory, Los Alamos, New Mexico 87545, USA*

(Received 16 March 2023; accepted 15 May 2023; published 2 June 2023)

We apply the adiabatic-nuclei molecular convergent close-coupling (MCCC) method to the study of elastic scattering and rotational excitation of H_2 by 0.01–20-eV electrons. Integral cross sections are presented for all rotational transitions with $|\Delta N| \leqslant 2$ and $N_i = 0$–31 within the $v = 0$ vibrational level and differential cross sections for a selection of transitions. Agreement with the available measurements and previous calculations is mostly excellent, depending on the transition and incident energy. We suggest possible reasons, and argue for the accuracy of the MCCC data.

DOI: 10.1103/PhysRevA.107.062804

I. INTRODUCTION

The problem of low-energy electron-impact rotational excitation of H_2 has been studied in great detail over the last 60 years due to its importance in low-temperature hydrogen plasmas and gasses. Below 10 eV, rotational excitation comprises up to 20% of the total cross section, and below the $v = 0 \rightarrow 1$ threshold ($\approx$0.5 eV) it is the dominant contribution to electron energy loss [1]. Accurate cross sections for the rotational transitions of H_2 are vital for modeling the emission spectra of astrophysical clouds [2] or for constructing collisional-radiative (CR) models of fusion-relevant plasmas [3]. Up to 0.5 eV, the $N = 0 \rightarrow 2$ and $1 \rightarrow 3$[1] rotational excitation cross sections are well known, with good agreement between the results of electron swarm experiments, which are reproduced by several calculations. At higher energies the situation is less ideal, with substantial disagreement between various measurements and calculations (and from the experimental side only the $N = 1 \rightarrow 3$ transition has been studied). A complete summary of the previous work is given later in in Sec. IV A.

The theoretical techniques applied to this problem have utilized a variety of approximations to the treatment of coupling between rovibrational levels, from the adiabatic-nuclei (AN) approximation in which the coupling is neglected, to the most accurate rovibrational close-coupling (RVCC) approach. However, the common factor in all previous studies is the use of model interaction potentials in place of coupling to the closed electronically inelastic channels. The somewhat arbitrary choice of model potentials can lead to differences in the calculated cross sections far more significant than the errors introduced by the AN approximation, particularly since the greatest discrepancies are at energies more than ten times the threshold energy, where the AN approximation is accurate [4]. What is clearly missing from the literature are theoretical studies of low-energy rotational excitation in which the coupling to closed electronic channels is accounted for rigorously. Although doing so while also coupling the electronic and nuclear motions would be computationally exhausting, the application of the AN approximation makes such an approach feasible, provided one can solve the electronic scattering problem accurately. In this paper we apply the molecular convergent close-coupling (MCCC) method, which in recent years has been shown to completely solve the electronic scattering problem for H_2 [5,6].

Over the past few years, the MCCC method has been applied within the AN approximation to produce a comprehensive set of vibrationally resolved cross sections for electrons scattering on H_2 and its isotopologues [7–10]. Application of the MCCC cross sections in a CR model for H_2 showed them to be much more accurate than previously available data when comparing predicted and measured population densities [11]. Recently, we have also applied the MCCC method to the calculation of rotationally resolved cross sections for the $X\,^1\Sigma_g^+ \rightarrow d\,^3\Pi_u$ excitation in order to study the polarization of Fulcher-α fluorescence [12], finding good agreement with measured linear polarization fractions for the $Q(1)$, $R(1)$, and $Q(3)$ transitions. We now turn our attention to rotationally resolved transitions within the $X\,^1\Sigma_g^+$ state, with an initial focus on those in which the vibrational quantum number does not change. Here we shall present integral and differential cross sections for rotationally elastic scattering and a number of rotational excitations, with comparison made against the available theory and experiment in the literature. The set of all rotational transitions within the $X\,^1\Sigma_g^+(v = 0)$ state with $|\Delta N| \leqslant 2$ are available online [13] (transitions with $|\Delta N| > 2$ have negligible cross sections by comparison). Atomic units are used throughout this paper unless specified otherwise.

II. THEORY

In this section we provide an overview of the theory of molecular structure and rotationally resolved scattering

*liam.scarlett@protonmail.com

[1]In the present work we apply Hund's angular-momentum coupling case (b), where the rotational levels are specified by the quantum number N.

applied in the present work. Further details can be found in Ref. [14]. Although considerable simplifications can be made to the theory in the case of transitions within a Σ state (zero electronic orbital-angular-momentum projection Λ on the internuclear axis), we present the theory here in the most general case as a reference for future applications to rotationally resolved scattering between electronic states of nonzero Λ.

A. Molecular structure

We represent the rovibronic target states in the nonrelativistic Born-Oppenheimer approximation, and utilize the LS and Hund's case (b) coupling schemes, which are appropriate for light diatomics such as H_2 [15]. A detailed description of the diatomic structure and formation of the total molecular wave functions in the present approximation scheme is given in Ref. [15], and the results are simply stated here. The total molecular state (neglecting nuclear spin) for a given electronic state n, vibrational level v, total orbital angular momentum (electronic and nuclear) N and its laboratory-frame projection m_N, and total parity π is given by

$$\Phi^{|\Lambda|tsm_s}_{nvNm_N\pi}(x_1, x_2, \boldsymbol{R}) = X^{m_s}_s(\sigma_1, \sigma_2)\Phi^{|\Lambda|ts}_{nvNm_N\pi}(\boldsymbol{r}_1, \boldsymbol{r}_2, \boldsymbol{R}), \quad (1)$$

where $x_i = (\sigma_i, \boldsymbol{r}_i)$ are the electron spin and spatial coordinates, $\boldsymbol{R}$ is the internuclear vector, and $X^{m_s}_s$ is the two-electron spin function (with total spin s and laboratory-frame projection m_s):

$$X^{m_s}_s(\sigma_1, \sigma_2) = \sum_{m_1 m_2} C^{sm_s}_{\frac{1}{2}m_1,\frac{1}{2}m_2}\chi_{m_1}(\sigma_1)\chi_{m_2}(\sigma_2), \quad (2)$$

with $C^{jm}_{j_1m_1,j_2m_2}$ being a Clebsch-Gordan coefficient. The spatial wave function is given by

$$\Phi^{|\Lambda|ts}_{nvNm_N\pi}(\boldsymbol{r}_1, \boldsymbol{r}_2, \boldsymbol{R}) = \frac{1}{\sqrt{2(1+\delta_{\Lambda,0})}}\left[\Phi^{|\Lambda|ts}_n(\boldsymbol{r}_1, \boldsymbol{r}_2; R)\phi^{|\Lambda|}_{Nm_N}(\hat{\boldsymbol{R}})\nu_{nvN}(R) + \pi(-1)^{N+\rho}\Phi^{-|\Lambda|ts}_n(\boldsymbol{r}_1, \boldsymbol{r}_2; R)\phi^{-|\Lambda|}_{Nm_N}(\hat{\boldsymbol{R}})\nu_{nvN}(R)\right]. \quad (3)$$

Here, $\Phi^{\Lambda ts}_n$ is the spatial wave function for the electronic state n with parity t, spin s, and orbital-angular-momentum projection Λ (on the rotating internuclear axis), and ν_{vnN} and $\phi^{\Lambda}_{Nm_N}$ are respectively the vibrational and rotational wave functions. Note that we define the index n such that it specifies the electronic state up to the sign of Λ so that we can explicitly distinguish the degenerate states $\Phi^{|\Lambda|}_n$ and $\Phi^{-|\Lambda|}_n$. As can be seen in Eq. (3), when Λ is nonzero the total molecular states are formed by a linear combination of the $|\Lambda|$ and $-|\Lambda|$ wave functions. The variable ρ is defined to be 1 for Σ^- states and 0 otherwise.

In the MCCC method the electronic target space is represented by a set of pseudostates which diagonalize the electronic Hamiltonian, as described in detail in Ref. [16]. The vibrational wave functions are the solutions to the following Schrödinger equation:

$$\left[-\frac{1}{2\mu}\frac{d^2}{dR^2} + \frac{N(N+1)-\Lambda^2}{2\mu R^2} + \epsilon_n(R)\right]\nu_{nvN}(R) = \varepsilon_{nvN}\nu_{nvN}(R), \quad (4)$$

which illustrates their dependence on the electronic and rotational states via the electronic potential-energy curve ϵ_n and the appearance of the rotational quantum number N in the centrifugal term. The rotational wave functions are given analytically by

$$\phi^{\Lambda}_{Nm_N}(\hat{\boldsymbol{R}}) = \sqrt{\frac{2N+1}{8\pi^2}}D^{N*}_{m_N,\Lambda}(\hat{\boldsymbol{R}}), \quad (5)$$

where $D^{N*}_{m_N,\Lambda}$ is a Wigner D function, and we adopt the convention that $\hat{\boldsymbol{R}}$, when used as an argument to the Wigner D function, is short for the set of Euler angles (α, β, γ) representing the coordinate transformation that aligns the laboratory-frame z axis with the internuclear axis.

In Hund's case (b) we refer to different rotational levels by the N quantum number, but since N also contains a contribution from Λ, it is not always indexed from 0. For example, Π states have N ranging from 1 upwards. In general, $N \geqslant |\Lambda|$. For electronic states of nonzero spin s, each rotational level is split into levels of different total angular momentum J, with $|N-s| \leqslant J \leqslant N+s$. Under the present set of approximations, the levels of the same N but different J are degenerate, and the spin-averaged cross sections we calculate here are summed (averaged) over the final (initial) J. For singlet states such as the $X\,^1\Sigma^+_g$ state of H_2, the N and J quantum numbers are equivalent; however, we use N at present for consistency with future work involving triplet states.

For homonuclear diatomics such as H_2 (and D_2 and T_2, but not the mixed isotopologues HD, HT, and DT), the total molecular wave function must be antisymmetric with respect to nuclear permutation when the nuclei are fermions (e.g., protons or tritons) and symmetric for bosons (e.g., deuterons). This requirement places a restriction on the allowed combinations of nuclear spin I and total molecular parity π. Furthermore, for the $\Sigma^\pm$ states ($\Lambda = 0$), the rotational quantum number N is constrained to always be even, or always odd, depending on the electronic symmetry and nuclear spin state. For states with nonzero Λ, the rotational levels are split into pairs of opposite parities $\pm\pi$, and it is conventional to label the states as $\Lambda^\pm$ (with $\Lambda = \Pi, \Delta$, and so on), where the Λ^+ states have $\pi=(-1)^N$ and the Λ^- states have $\pi=(-1)^{N+1}$. Hence, although the $\pm$ superscript on the $\Lambda \neq 0$ states does not carry the same physical meaning as for the Σ states (where it relates to symmetry under inversion through a plane containing the internuclear axis), the constraints placed on N and π are the same. In Table I we summarize these constraints for the different combinations of electronic symmetries, nuclear spin states, and fermionic/bosonic nuclei. Since we assume there is no ortho/para conversion in the collision, these rules determine the allowed rotational transitions. For the simple case of transitions within the $X\,^1\Sigma^+_g$ state of H_2 in the present study, we have that para-H_2 must always have even rotational levels, and ortho always odd.

TABLE I. Constraints on the quantum number N and total molecular parity π for homonuclear diatomics given the electronic symmetry $\Lambda_t^{\pm}$ and either fermionic or bosonic nuclei in the ortho or para nuclear spin configurations. Note that t refers to the electronic parity.

		Fermions		Bosons	
	$\Lambda_t^{\pm}$	$(-1)^N$	π	$(-1)^N$	π
Ortho ($I=1$):	Λ_g^+	−	−	+	+
	Λ_g^-	+	−	−	+
	Λ_u^+	+	+	−	−
	Λ_u^-	−	+	+	−
Para ($I=0$):	Λ_g^+	+	+	−	−
	Λ_g^-	−	+	+	−
	Λ_u^+	−	−	+	+
	Λ_u^-	+	−	−	+

B. Partial-wave expansion

The projectile wave function (plane wave) is expanded in partial waves of well-defined orbital angular momentum L and its projection m_L on the laboratory-frame z axis:

$$|\boldsymbol{q}\rangle = \frac{1}{q}\sum_{Lm_L} i^L |qLm_L\rangle Y_L^{m_L*}(\hat{\boldsymbol{q}})\big|\tfrac{1}{2}m\big\rangle, \tag{6}$$

where $\boldsymbol{q}$ is the linear momentum (equivalently the wave vector in atomic units where $\hbar = 1$), $Y_L^{m_L*}$ is a spherical harmonic, m is the spin projection on the laboratory-frame z axis, and $|qLm_L\rangle$ are defined by

$$\langle \boldsymbol{r}|qLm_L\rangle = \sqrt{\frac{2}{\pi}}\frac{1}{r}u_L(qr)Y_L^{m_L}(\hat{\boldsymbol{r}}), \tag{7}$$

with u_L being Riccati-Bessel functions for nondistorted plane waves. We represent the asymptotic projectile-target states in coupled-angular-momentum form by expanding in partial waves of total-scattering-system orbital angular momentum $\mathcal{J}$, parity Π, and spin $\mathcal{S}$:

$$\big|\Phi^{|\Lambda|tsm_s}_{nvNm_N\pi}\,\boldsymbol{q}\big\rangle = \frac{1}{q}\sum_{Lm_L} i^L \big|\Phi^{|\Lambda|tsm_s}_{nvNm_N\pi}\big\rangle |qLm_L\rangle Y_L^{m_L*}(\hat{\boldsymbol{q}})\big|\tfrac{1}{2}m\big\rangle \tag{8}$$

$$= \sum_{\mathcal{J}\Pi\mathcal{S}}\sum_{Lm_L} C^{\mathcal{J}M_\mathcal{J}}_{Lm_L,Nm_N} C^{\mathcal{S}M_\mathcal{S}}_{\frac{1}{2}m,sm_s} Y_L^{m_L*}(\hat{\boldsymbol{q}}) \times |nvN\pi\; qL:\mathcal{J}M_\mathcal{J}\Pi\mathcal{S}M_\mathcal{S}\rangle, \tag{9}$$

where

$$|nvN\pi\; qL:\mathcal{J}M_\mathcal{J}\Pi\mathcal{S}M_\mathcal{S}\rangle = \frac{1}{q}i^L \sum_{m_Lm_Nmm_s} C^{\mathcal{J}M_\mathcal{J}}_{Lm_L,Nm_N} C^{\mathcal{S}M_\mathcal{S}}_{\frac{1}{2}m,sm_s} \big|\Phi^{|\Lambda|tsm_s}_{nvNm_N\pi}\big\rangle\big|qLm_L\big\rangle\big|\tfrac{1}{2}m\big\rangle. \tag{10}$$

The projections m, m_s, m_L, m_N, $M_\mathcal{J}$, and $M_\mathcal{S}$ are all with respect to the laboratory-frame z axis, and note that the target variables $|\Lambda|$, t, and s are neglected on the left-hand side of Eq. (10), as they are determined by the electronic-state index n.

Following Eqs. (8) and (10), the scattering amplitude for a transition fully resolved in angular-momentum and spin sublevels is given by

$$F_{n_fv_fN_fm_{N_f}\pi_fm_fm_{s_f},n_iv_iN_im_{N_i}\pi_im_im_{s_i}}(\boldsymbol{q}_f,\boldsymbol{q}_i) = \sum_{\mathcal{S}} C^{\mathcal{S}M_\mathcal{S}}_{\frac{1}{2}m_f,s_fm_{s_f}} C^{\mathcal{S}M_\mathcal{S}}_{\frac{1}{2}m_i,s_im_{s_i}} F^{\mathcal{S}}_{n_fv_fN_fm_{N_f}\pi_f,n_iv_iN_im_{N_i}\pi_i}(\boldsymbol{q}_f,\boldsymbol{q}_i), \tag{11}$$

$$F^{\mathcal{S}}_{n_fv_fN_fm_{N_f}\pi_f,n_iv_iN_im_{N_i}\pi_i}(\boldsymbol{q}_f,\boldsymbol{q}_i) = \sum_{\mathcal{J}\Pi}\sum_{\substack{L_fL_i\\ m_{L_f}}} \frac{\hat{L}_i}{\sqrt{4\pi}} C^{\mathcal{J}M_\mathcal{J}}_{L_fm_{L_f},N_fm_{N_f}} C^{\mathcal{J}M_\mathcal{J}}_{L_i0,N_im_{N_i}} Y_{L_f}^{m_{L_f}}(\hat{\boldsymbol{q}}_f) F^{\mathcal{J}\Pi\mathcal{S}}_{n_fv_fN_f\pi_fL_f,n_iv_iN_i\pi_iL_i}(q_f,q_i), \tag{12}$$

where $\hat{L} = \sqrt{2L+1}$, and we have assumed the laboratory-frame z axis is aligned with the incident beam. The laboratory-frame partial-wave scattering amplitudes are defined by

$$F^{\mathcal{J}\Pi\mathcal{S}}_{n_fv_fN_f\pi_fL_f,n_iv_iN_i\pi_iL_i}(q_f,q_i) = -(2\pi)^2\langle q_fL_f\, n_fv_fN_f\pi_f||T^{\mathcal{J}\Pi\mathcal{S}}||n_iv_fN_i\pi_i\, q_iL_i\rangle, \tag{13}$$

where we have applied the Wigner-Eckart theorem [17] to remove the dependence on $M_\mathcal{J}$ and $M_\mathcal{S}$. In the present work the AN approximation is applied to the calculation of the reduced partial-wave T-matrix elements in the right-hand side of Eq. (13), and we expand on this in Sec. II C. However, the expressions for the differential and integrated cross sections in the following sections hold true regardless of the method by which the partial-wave scattering amplitudes are obtained.

C. Adiabatic-nuclei approximation

We invoke the AN approximation to decouple the electronic, vibrational, and rotational degrees of freedom. At present, we limit our study to transitions in which the vibrational quantum number v remains unchanged. Since the vibrationally elastic cross sections are not much affected by resonance effects, the error associated with neglecting coupling between vibrational levels will not be substantial. Future work can be directed towards the calculation of vibrationally inelastic cross sections using the vibrational and electronic close-coupling variation of the MCCC method recently developed by Scarlett *et al.* [18]. Based on previous comparisons of AN and RVCC calculations [4], the error introduced by neglecting the coupling between rotational levels is not important except at energies very close to threshold.

With the electronic and nuclear motions decoupled, the electronic scattering problem is solved most conveniently in the body frame, in which the z axis is aligned with the internuclear axis (and is hence no longer fixed in space). After expanding the body-frame electronic scattering amplitudes in partial waves with conserved-scattering-system total electronic-angular-momentum projection Λ_e, electronic parity Π_e, projectile angular momentum L, and its projection on the internuclear axis Λ_L, the laboratory-frame partial-wave amplitudes (13) can be expressed in terms of body-frame partial-wave amplitudes by

$$
\begin{aligned}
F^{\mathcal{J}\Pi\mathcal{S}}_{n_f v_f N_f \pi_f L_f, n_i v_i N_i \pi_i L_i}(q_f, q_i) = {} & \frac{\hat{N}_f \hat{N}_i i^{L_i - L_f}}{\sqrt{2(1+\delta_{\Lambda_f,0})}\sqrt{2(1+\delta_{\Lambda_i,0})}} \frac{1}{\hat{\mathcal{J}}^2} \int dR\, v_{n_f v_f N_f}(R)\, v_{n_i v_i N_i}(R), \\
& \times \sum_{\Lambda_e \Pi_e} \sum_{\Lambda_{L_f} \Lambda_{L_i}} \Big[C^{\mathcal{J}\Lambda_e}_{L_f \Lambda_{L_f}, N_f |\Lambda_f|}\, C^{\mathcal{J}\Lambda_e}_{L_i \Lambda_{L_i}, N_i |\Lambda_i|}\, F^{\Lambda_e \Pi_e \mathcal{S}}_{n_f |\Lambda_f| L_f \Lambda_{L_f}, n_i |\Lambda_i| L_i \Lambda_{L_i}}\left(q_f^{\mathrm{FN}}, q_i, R\right) \\
& + \pi_f (-1)^{N_f + \rho_f}\, C^{\mathcal{J}\Lambda_e}_{L_f \Lambda_{L_f}, N_f (-|\Lambda_f|)}\, C^{\mathcal{J}\Lambda_e}_{L_i \Lambda_{L_i}, N_i |\Lambda_i|}\, F^{\Lambda_e \Pi_e \mathcal{S}}_{n_f (-|\Lambda_f|) L_f \Lambda_{L_f}, n_i |\Lambda_i| L_i \Lambda_{L_i}}\left(q_f^{\mathrm{FN}}, q_i, R\right) \\
& + \pi_i (-1)^{N_i + \rho_i}\, C^{\mathcal{J}\Lambda_e}_{L_f \Lambda_{L_f}, N_f |\Lambda_f|}\, C^{\mathcal{J}\Lambda_e}_{L_i \Lambda_{L_i}, N_i (-|\Lambda_i|)}\, F^{\Lambda_e \Pi_e \mathcal{S}}_{n_f |\Lambda_f| L_f \Lambda_{L_f}, n_i (-|\Lambda_i|) L_i \Lambda_{L_i}}\left(q_f^{\mathrm{FN}}, q_i, R\right) \\
& + \pi_f \pi_i (-1)^{N_f + N_i + \rho_f + \rho_i}\, C^{\mathcal{J}\Lambda_e}_{L_f \Lambda_{L_f}, N_f (-|\Lambda_f|)}\, C^{\mathcal{J}\Lambda_e}_{L_i \Lambda_{L_i}, N_i (-|\Lambda_i|)}\, F^{\Lambda_e \Pi_e \mathcal{S}}_{n_f (-|\Lambda_f|) L_f \Lambda_{L_f}, n_i (-|\Lambda_i|) L_i \Lambda_{L_i}}\left(q_f^{\mathrm{FN}}, q_i, R\right) \Big],
\end{aligned}
\tag{14}
$$

where q_f^{FN} is the fixed-nuclei outgoing momentum corresponding to the R-dependent vertical electronic excitation energy rather than the physical rovibrationally resolved excitation energy. This variable is present in Eq. (14) to indicate that the body-frame electronic scattering amplitudes are on the energy shell within the fixed-nuclei formalism but violate energy conservation when one considers the rovibronic excitation energies. Morrison *et al.* [4] discussed this issue at length and developed the first-order nondegenerate adiabatic (FONDA) method, which uses electronic scattering amplitudes which are "off shell" within the fixed-nuclei picture but satisfy the physical energy conservation requirement. Since off-shell amplitudes cannot be obtained using the MCCC method, we do not adopt this approach; however, these considerations are important only near threshold energies. Furthermore, when defining the cross sections in the following sections, we retain the physical (rovibrationally resolved) q_f in the flux factor, which ensures the cross sections go to zero at the correct threshold.

As described in Ref. [16], the body-frame scattering amplitudes are obtained by solving the partial-wave coupled Lippmann-Schwinger equations in prolate spheroidal coordinates (for better target-structure accuracy) and converted to spherical coordinates at each fixed internuclear separation before the integration over R is performed in Eq. (14). In the electronic body-frame scattering calculations, the degenerate pairs of electronic states with nonzero Λ each appear as two distinct states in the close-coupling expansion. The amplitudes with different combinations of $\pm|\Lambda_f|$ and $\pm|\Lambda_i|$ appear in the four separate terms in Eq. (14). This follows directly from the definition of the total molecular states (3) as a linear combination of the $\pm|\Lambda|$ electronic states. In the present work we are concerned only with rotational transitions within the $X\,{}^1\Sigma_g^+$ state of H_2, and hence $\Lambda_f = \Lambda_i = 0$, and the above simplifies considerably. However, we keep the theory here as general as possible for future reference when further work is directed towards studies of rotationally resolved, electronically inelastic scattering.

D. Differential cross sections

The spin-averaged differential cross section (DCS) resolved in rotational sublevels is given by

$$
\begin{aligned}
&\frac{d\sigma_{n_f v_f N_f m_{N_f} \pi_f, n_i v_i N_i m_{N_i} \pi_i}}{d\Omega} \\
&= \sum_{\mathcal{S}} \frac{2\mathcal{S}+1}{2(2s_i+1)} \sum_{L} A^{L\mathcal{S}}_{n_f v_f N_f m_{N_f} \pi_f, n_i v_i N_i m_{N_i} \pi_i} P_L(\cos\theta),
\end{aligned}
\tag{15}
$$

where P_L is a Legendre polynomial, and

$$
\begin{aligned}
A^{L\mathcal{S}}_{n_f v_f N_f m_{N_f} \pi_f, n_i v_i N_i m_{N_i} \pi_i} = {} & \frac{q_f}{q_i} \frac{(-1)^{m_{N_i} - m_{N_f}}}{(4\pi)^2} \sum_{\mathcal{J}\Pi\mathcal{J}'\Pi'} \sum_{L_f L_f'} \sum_{L_i L_i'} \hat{L}_f \hat{L}_f' \hat{L}_i \hat{L}_i' F^{\mathcal{J}\Pi\mathcal{S}}_{n_f v_f N_f \pi_f L_f, n_i v_i N_i \pi_i L_i}(q_f, q_i) F^{\mathcal{J}'\Pi'\mathcal{S}*}_{n_f v_f N_f \pi_f L_f', n_i v_i N_i \pi_i L_i'}(q_f, q_i) \\
& \times C^{\mathcal{J} m_{N_i}}_{L_i 0, N_i m_{N_i}}\, C^{\mathcal{J}' m_{N_i}}_{L_i' 0, N_i m_{N_i}}\, C^{L0}_{L_f (m_{N_i} - m_{N_f}), L_f' (m_{N_f} - m_{N_i})}\, C^{L0}_{L_f 0, L_f' 0}\, C^{\mathcal{J} m_{N_i}}_{L_f (m_{N_i} - m_{N_f}), N_f m_{N_f}}\, C^{\mathcal{J}' m_{N_i}}_{L_f' (m_{N_i} - m_{N_f}), N_f m_{N_f}}.
\end{aligned}
\tag{16}
$$

The DCS summed over m_{N_f} and averaged over m_{N_i} is given by a similar expression to Eq. (15), with

$$A^{L\mathcal{S}}_{n_f v_f N_f \pi_f, n_i v_i N_i \pi_i} = \frac{q_f}{q_i}\frac{(-1)^{N_f+N_i}}{\hat{N}_i^2(4\pi)^2}\sum_{\mathcal{J}\Pi\mathcal{J}'\Pi'}\sum_{L_f L_f'}\sum_{L_i L_i'}\hat{\mathcal{J}}^2\hat{\mathcal{J}}'^2\hat{L}_f\hat{L}_f'\hat{L}_i\hat{L}_i' F^{\mathcal{J}\Pi\mathcal{S}}_{n_f v_f N_f \pi_f L_f, n_i v_i N_i \pi_i L_i}(q_f, q_i)$$
$$\times F^{\mathcal{J}'\Pi'\mathcal{S}*}_{n_f v_f N_f \pi_f L_f', n_i v_i N_i \pi_i L_i'}(q_f, q_i) C^{L0}_{L_f 0, L_f' 0} C^{L0}_{L_i 0, L_i' 0}\begin{Bmatrix} L_f' & N_f & \mathcal{J}' \\ \mathcal{J} & L & L_f \end{Bmatrix}\begin{Bmatrix} L_i' & N_i & \mathcal{J}' \\ \mathcal{J} & L & L_i \end{Bmatrix}, \tag{17}$$

where $\begin{Bmatrix} j_1 & j_2 & j_3 \\ j_4 & j_5 & j_6 \end{Bmatrix}$ are the Wigner $6j$ symbols.

E. Integrated cross sections

After integrating the DCS over a solid angle only the $L = 0$ term of the Legendre expansion remains, and we obtain

$$\sigma_{n_f v_f N_f \pi_f m_{N_f}, n_i v_i N_i \pi_i m_{N_i}} = \sum_{\mathcal{S}}\frac{2\mathcal{S}+1}{2(2s_i+1)}\frac{q_f}{q_i}\frac{1}{4\pi}\sum_{\mathcal{J}\Pi\mathcal{J}'\Pi'}\sum_{L_f}\sum_{L_i L_i'}\hat{L}_i\hat{L}_i' F^{\mathcal{J}\Pi\mathcal{S}}_{n_f v_f N_f \pi_f L_f, n_i v_i N_i \pi_i L_i}(q_f, q_i) F^{\mathcal{J}'\Pi'\mathcal{S}*}_{n_f v_f N_f \pi_f L_f, n_i v_i N_i \pi_i L_i'}(q_f, q_i)$$
$$\times C^{\mathcal{J} m_{N_i}}_{L_i 0, N_i m_{N_i}} C^{\mathcal{J}' m_{N_i}}_{L_i' 0, N_i m_{N_i}} C^{\mathcal{J} m_{N_i}}_{L_f (m_{N_i} - m_{N_f}), N_f m_{N_f}} C^{\mathcal{J}' m_{N_i}}_{L_f (m_{N_i} - m_{N_f}), N_f m_{N_f}} \tag{18}$$

for the spin-averaged integrated cross section (ICS) resolved in rotational sublevels, and

$$\sigma_{n_f n_v N_f \pi_f, n_i v_i N_i \pi_i} = \sum_{\mathcal{S}}\frac{2\mathcal{S}+1}{2(2s_i+1)}\frac{q_f}{4\pi q_i \hat{N}_i^2}\sum_{\mathcal{J}\Pi}\sum_{L_f L_i}\hat{\mathcal{J}}^2\left|F^{\mathcal{J}\Pi\mathcal{S}}_{n_f v_f N_f \pi_f L_f, n_i v_i N_i \pi_i L_i}(q_f, q_i)\right|^2 \tag{19}$$

for the ICS summed (averaged) over the final (initial) rotational sublevels.

F. Analytic Born completion

To accelerate the convergence of the calculated cross sections with respect to the maximum projectile angular momentum L included in the partial-wave expansion, we employ the analytic Born completion (ABC) method. The energies considered in the present work (up to 20 eV) can be several hundred times the rotationally inelastic threshold (0.044 eV), which leads to slow partial-wave convergence of the inelastic DCS. The application of the ABC method to nonrotationally resolved scattering in the MCCC method has been detailed previously [19]. In the present case, the rotationally resolved analytic Born amplitude is expanded in partial waves as

$$F^{(\mathrm{AB})}_{n_f v_f N_f m_{N_f} \pi_f, n_i v_i N_i m_{N_i} \pi_i}(\boldsymbol{Q}) = \sum_{\lambda} V^{\lambda}_{n_f v_f N_f \pi_f, n_i v_i N_i \pi_i}(Q) C^{\lambda(m_{N_f} - m_{N_i})}_{N_f(-m_{N_f}), N_i m_{N_i}} Y_{\lambda}^{m_{N_f} - m_{N_i}}(\hat{\boldsymbol{Q}}), \tag{20}$$

where

$$V^{\lambda}_{n_f v_f N_f \pi_f, n_i v_i N_i \pi_i}(Q) = \frac{-(2\pi)^2 \hat{N}_f \hat{N}_i i^{\lambda}(-1)^{m_{N_i}+|\Lambda_i|}}{\sqrt{2(1+\delta_{\Lambda_f,0})}\sqrt{2(1+\delta_{\Lambda_i,0})}}\frac{1}{\hat{\lambda}^2}\int dR v_{n_f v_f N_f}(R)\, v_{n_i v_i N_i}(R)\Big[V^{\lambda}_{n_f N_f|\Lambda_f|, n_i N_i|\Lambda_i|}(Q, R)$$
$$+ \pi_f(-1)^{N_f+\rho_f} V^{\lambda}_{n_f N_f(-|\Lambda_f|), n_i N_i|\Lambda_i|}(Q, R) + \pi_i(-1)^{N_i+\rho_i} V^{\lambda}_{n_f N_f|\Lambda_f|, n_i N_i(-|\Lambda_i|)}(Q, R)$$
$$+ \pi_f\pi_i(-1)^{N_f+N_i+\rho_f+\rho_i} V^{\lambda}_{n_f N_f(-|\Lambda_f|), n_i N_i(-|\Lambda_i|)}(Q, R)\Big], \tag{21}$$

and

$$V^{\lambda}_{n_f N_f \Lambda_f, n_i N_i \Lambda_i}(Q, R) = C^{\lambda(\Lambda_f - \Lambda_i)}_{N_f \Lambda_f, N_i(-\Lambda_i)} V^{\lambda}_{n_f \Lambda_f, n_i \Lambda_i}(Q, R). \tag{22}$$

Here, $V^{\lambda}_{n_f \Lambda_f, n_i \Lambda_i}$ are the body-frame electronic Born matrix elements defined in Eq. (104) of Ref. [19], and $\boldsymbol{Q} = \boldsymbol{q}_i - \boldsymbol{q}_f$ is the momentum-transfer vector. The Born DCS and ICS are then given by

$$\frac{d\sigma^{(\mathrm{AB})}_{n_f v_f N_f m_{N_f} \pi_f, n_i v_i N_i m_{N_i} \pi_i}}{d\Omega} = \frac{q_f}{q_i}\left|F^{(\mathrm{AB})}_{n_f v_f N_f m_{N_f} \pi_f, n_i v_i N_i m_{N_i} \pi_i}(\boldsymbol{Q})\right|^2 \tag{23}$$

$$\sigma^{(\mathrm{AB})}_{n_f v_f N_f m_{N_f} \pi_f, n_i v_i N_i m_{N_i} \pi_i} = 2\pi\int \frac{d\sigma^{(\mathrm{AB})}_{n_f v_f N_f m_{N_f} \pi_f, n_i v_i N_i m_{N_i} \pi_i}}{d\Omega}\sin\theta d\theta, \tag{24}$$

where the scattering angle θ is related to the angle $\theta_{\hat{\boldsymbol{Q}}}$ between $\hat{\boldsymbol{Q}}$ and $\hat{\boldsymbol{q}}_i$ by

$$\theta_{\hat{\boldsymbol{Q}}} = \arccos[(q_i - q_f\cos\theta)/Q]. \tag{25}$$

The integration over θ in Eq. (24) is performed numerically.

The ABC procedure for the DCS is applied to the amplitude $F^{\mathcal{S}}$ defined in Eq. (12), with the ABC amplitude

defined as

$$F^{\mathcal{S}\,(\mathrm{ABC})}_{n_f v_f N_f m_{N_f} \pi_f, n_i v_i N_i m_{N_i} \pi_i}(\boldsymbol{q}_f, \boldsymbol{q}_i) = F^{\mathcal{S}}_{n_f v_f N_f m_{N_f} \pi_f, n_i v_i N_i m_{N_i} \pi_i}(\boldsymbol{q}_f, \boldsymbol{q}_i) - F^{(\mathrm{PWB})}_{n_f v_f N_f m_{N_f} \pi_f, n_i v_i N_i m_{N_i} \pi_i}(\boldsymbol{q}_f, \boldsymbol{q}_i) + F^{(\mathrm{AB})}_{n_f v_f N_f m_{N_f} \pi_f, n_i v_i N_i m_{N_i} \pi_i}(\boldsymbol{Q}), \tag{26}$$

where $F^{(\mathrm{PWB})}$ is the Born amplitude calculated using the same projectile partial-wave expansion as F^{S} [by replacing the T-matrix elements used to obtain the body-frame partial-wave amplitudes in Eq. (14) with the direct-only V-matrix elements]. In order for $F^{(\mathrm{AB})}$ to be calculated in a way which is consistent with the calculation of $F^{(\mathrm{PWB})}$ and $F^{\mathcal{S}}$, where the electronically elastic amplitudes assume $q_f = q_i$, we must evaluate $\boldsymbol{Q}$ with the same assumption (i.e., by making the approximation $\boldsymbol{Q} \approx q_i \hat{\boldsymbol{q}}_f - \boldsymbol{q}_i$). Otherwise, the mismatch between $F^{(\mathrm{AB})}$ and $F^{(\mathrm{PWB})}$ can create issues at small scattering angles. Since we are presenting the theory in a way which can be applied generally to transitions between any electronic states, it is worth noting that for electronically inelastic scattering one should replace $\boldsymbol{Q}$ with the R-dependent momentum-transfer vector calculated using the vertical excitation energy [and hence move the spherical harmonic in Eq. (20) inside the integration over R in Eq. (21)]. However, since the electronic excitation energies are large compared to the rovibrational energy spacings, the discrepancy between $F^{(\mathrm{AB})}$ and $F^{(\mathrm{PWB})}$ for electronically inelastic scattering will be negligible and this issue can be ignored.

The spin-weighted ABC DCS is given by

$$\frac{d\sigma^{(\mathrm{ABC})}_{n_f v_f N_f m_{N_f} \pi_f, n_i v_i N_i m_{N_i} \pi_i}}{d\Omega} = \sum_{\mathcal{S}} \frac{2\mathcal{S}+1}{2(2s_i+1)} \frac{q_f}{q_i} \left| F^{\mathcal{S}\,(\mathrm{ABC})}_{n_f v_f N_f m_{N_f} \pi_f, n_i v_i N_i m_{N_i} \pi_i}(\boldsymbol{q}_f, \boldsymbol{q}_i) \right|^2, \tag{27}$$

and it is explicitly summed (averaged) over the final (initial) rotational sublevels as required. The ABC ICS can be obtained by integrating Eq. (27) over a solid angle, but it is sufficient to apply the ABC procedure directly to the ICS using

$$\sigma^{(\mathrm{ABC})}_{n_f v_f N_f \pi_f, n_i v_i N_i \pi_i} = \sigma_{n_f v_f N_f \pi_f, n_i v_i N_i \pi_i} - \sigma^{(\mathrm{PWB})}_{n_f v_f N_f \pi_f, n_i v_i N_i \pi_i} + \sigma^{(\mathrm{AB})}_{n_f v_f N_f \pi_f, n_i v_i N_i \pi_i}, \tag{28}$$

where, similarly to before, $\sigma^{(\mathrm{PWB})}$ is the Born ICS calculated using the same projectile partial-wave expansion used in the close-coupling calculations. In Fig. 1 we demonstrate the application of the ABC technique to the $N = 0 \to 2$ DCS at 1.0-eV incident energy (≈23 times the excitation threshold of 0.044 eV).

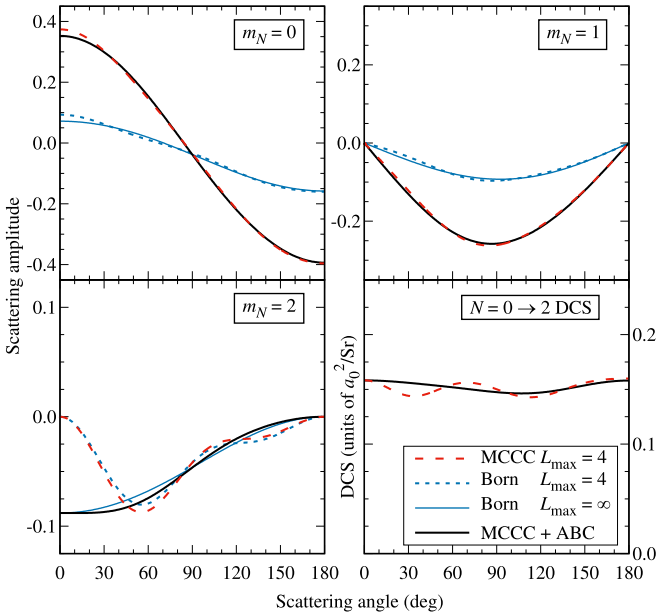

FIG. 1. Illustration of the analytical Born completion (ABC) procedure applied to the 1.0-eV $N = 0 \to 2$ DCS. In this case the $m_N = 0$ and 1 amplitudes $F^{\mathcal{S}}$ are converged well with $L_{\max} = 4$, but the $m_N = 2$ amplitude is not, leading to oscillations in the DCS. The oscillations are removed by applying the ABC procedure to account for partial waves up to infinity.

III. CALCULATION DETAILS

The electronic structure model we have adopted here is nearly identical to what was used in Ref. [16] but with a smaller number of correlation configurations constructed from the $1s$, $2s$, $2p$, $3d$, and $4f$ orbitals. (In Ref. [16] we added the $3s$, $3p$, and $4d$ orbitals for greater accuracy at the larger values of R spanned by the $v > 0$ vibrational wave functions.) In the close-coupling expansion we keep the first 301 electronic states out of the 465 generated using this model, corresponding to those with excitation energies up to 100 eV from the ground state. For the projectile partial-wave expansion we use a maximum angular momentum of $L_{\max} = 4$, with the ABC method applied to account for higher partial waves. These parameters are sufficient to achieve convergence in the electronically elastic ICS below the ionization threshold, as confirmed by comparison with the convergence studies of Savage [20]. While the rotationally elastic DCS do not suffer from the oscillatory behavior seen in Fig. 1 when the partial-wave expansion is unconverged, the absence of higher partial waves leads to incorrect behavior at forward scattering angles. The ABC procedure alone is unable to address this issue since elastic scattering is dominated by the effects of target polarization which are not accounted for in the first-order Born approximation. Therefore, when computing the rotationally elastic DCS, we top up the $L \leqslant 4$ amplitudes with approximate amplitudes calculated up to $L_{\max} = 40$ using a smaller seven-state close-coupling expansion, which is sufficient to account for 90% of the bound static dipole polarizability. This procedure corrects the forward scattering elastic DCS.

The electronic scattering calculations were performed at 40 incident energies between 0.01 and 20 eV, each with 18 evenly spaced R points between 0.8 and 2.5 a_0, covering the span of the $v = 0$ vibrational wave function. Each calculation took about one hour using 480 Intel Xeon Haswell E5-2690v3 2.6 GHz processor cores (20 nodes on the Pawsey Supercomputing Centre's *Magnus* machine), for a total of about

350,000 core hours spent on the electronic scattering calculations. The time spent on the subsequent AN calculations to produce rovibrationally resolved cross sections is insignificant by comparison.

IV. RESULTS

In this section, we present AN cross sections for rotational transitions within the $X\,^1\Sigma_g^+(v_i = 0)$ state of H_2. There are 32 rotational levels $N = 0 - 31$ for which the $v = 0$ vibrational wave function is bound, and hence there are 92 possible transitions with $\Delta N = 0, \pm 2$ (transitions with $\Delta N = \pm 4, \pm 6, \ldots$ are possible but with much smaller cross sections). Data files for the results presented here are available online [13].

A. Previous calculations and measurements

Rotationally elastic scattering and rotational excitation of H_2 by electron impact have been investigated previously in great detail, both by theory and experiment. In Table II we summarize the various theoretical and experimental studies with which we compare our calculations and specify the methods applied in each. Some older work is omitted from the table and our later comparisons where the results have already been shown to be inaccurate (e.g., the 1956 calculations of Massey and Ridley [21] were later shown to be inaccurate because they included only s-wave scattering [22]).

Early rotational close-coupling (RCC) calculations were performed in the late 1960s by Lane and Geltman [23] using the rigid-rotator (RR) approximation (fixed internuclear separation) and a model interaction potential (MIP) to account for target polarization. The effects of the exchange interaction were excluded, and hence, as stated by the authors, the molecule is represented by a rigid rotator with a polarizable charge distribution. Once the problem has been simplified to this point it is feasible to perform calculations with coupling between rotational excitation channels, i.e., without invoking the AN approximation. By contrast, a close-coupling calculation including rotational, vibrational, and electronic channel couplings would be computationally prohibitive even by today's standards (although recent work suggests this will soon change [18]). Subsequent work by Henry and Lane [22] employed the same approach but with the inclusion of exchange. This addition proved to make a substantial difference in the elastic and rotational excitation cross sections, and yielded much better agreement with experiment compared to the previous work.

Numerous studies have been performed since the above, up until the most recent calculations by Telega and Gianturco [24] in 2005. Some have utilized RCC, or even RVCC, and some have employed the AN approximation to neglect all couplings. Morrison and co-workers [4,25–27] have spent considerable time investigating the differences between RCC, RVCC, and AN calculations, suggesting corrections to the AN approximation such as the energy-modified adiabatic (EMA) and FONDA methods. The common factor among almost all previous calculations is the use of MIPs in place of a rigorous account of coupling to the closed electronically inelastic channels. In many cases the (somewhat arbitrary) choice of polarization and exchange potentials can lead to drastically different results between various calculations.

TABLE II. A summary of the various studies applied previously to electron-impact elastic scattering and rotational excitation of H_2 referred to in the present work. The acronyms for the theoretical methods are defined in the footnote to the table.

Reference	Year	Description
Calculations		
Lane and Geltman [23]	1967	RCC, RR, MIP
Henry and Lane [22]	1969	RCC, RR, MIP
Hara [30]	1969	AN, MIP
Lane and Geltman [31]	1969	Same as Ref. [23]
Henry [32]	1970	RVCC, MIP
Henry and Chang [33]	1972	RVCC, FT, MIP
Morrison *et al.* [25]	1984	RCC/AN/EMA, RR, MIP
Morrison and Saha [26]	1986	RVCC, MIP
Morrison *et al.* [27]	1987	RVCC, MIP
Trail *et al.* [34]	1990	VIBAV, MIP
Morrison *et al.* [4]	1991	FONDA, MIP
Telega *et al.* [35]	2004	RCC, MIP
Telega and Gianturco [24]	2005	RVCC, MIP
Experiment		
Ehrhardt and Linder [36]	1968	Beam
Crompton *et al.* [37]	1969	Swarm
Gibson [38]	1970	Swarm
Linder and Schmidt [39]	1971	Beam
Wong and Schultz [40]	1974	Beam
Ferch *et al.* [41]	1980	Beam
Furst *et al.* [42]	1984	Beam
Jones [43]	1985	Beam
England *et al.* [28]	1988	Swarm
Subramanian and Kumar [44]	1985	Beam

RCC: Rotational close-coupling
RVCC: Rovibrational close-coupling
RR: Rigid-rotator approximation
MIP: Model interaction potential
AN: Adiabatic-nuclei approximation
FT: Frame transformation method
VIBAV: Vibrationally averaged interaction potential
EMA: Energy-modified adiabatic
FONDA: First-order nondegenerate adiabatic

Several experiments were performed from the 1960s to 1980s. In Table II we have specified whether they are crossed-beam experiments (where the DCS is directly measured and integrated to produce the ICS) or swarm experiments (where the ICS is inferred from the analysis of transport coefficients derived from swarm data). As explained by England *et al.* [28], the rotational excitation cross sections can be uniquely derived from a swarm experiment only below the first vibrationally inelastic threshold at around 0.4 eV. Although England *et al.* [28] do present results up to 15 eV, the cross sections above 1.3 eV for $N = 1 \rightarrow 3$, and above 0.4 eV for $N = 0 \rightarrow 2$, $N = 2 \rightarrow 4$, and $N = 3 \rightarrow 5$, are in fact taken from calculations of Morrison *et al.* [27,29], and hence when presenting their results in the following sections we restrict them to energies corresponding to the actual measurements.

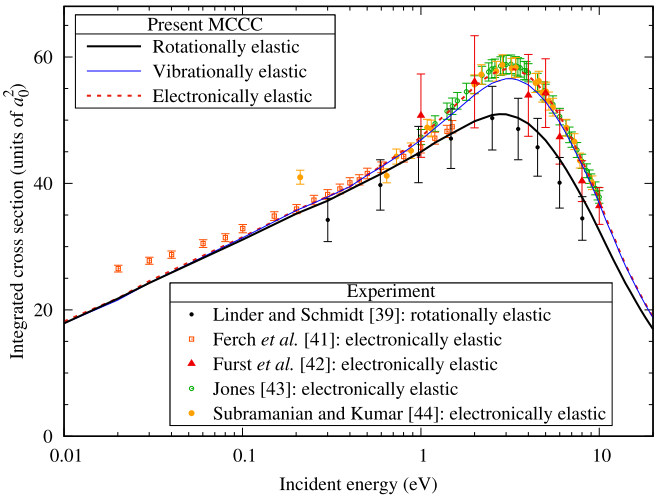

FIG. 2. Integrated cross sections for rotationally, vibrationally, and electronically elastic collisions with H_2. Comparison is made with the measurements of Linder and Schmidt [39], Ferch *et al.* [41], Furst *et al.* [42], Jones [43], and Subramanian and Kumar [44].

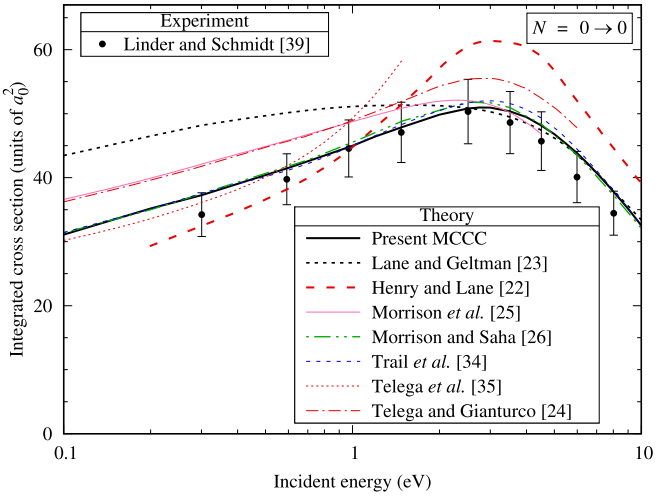

FIG. 3. Integrated cross section for rotationally elastic collisions with H_2. Comparison is made with the calculations of Henry and Lane [22], Lane and Geltman [23], Morrison *et al.* [25], Morrison and Saha [26], Trail *et al.* [34], Telega *et al.* [35], and Telega and Gianturco [24], and the measurements of Linder and Schmidt [39].

The calculations of Morrison *et al.* [27,29] are presented separately as theoretical results.

B. Elastic scattering

In Fig. 2 we present the integrated cross section(s) for elastic scattering on H_2. In principle, the term elastic scattering should refer only to transitions in which neither the rotational or vibrational quantum numbers change. However, the limits of energy resolution in experiments can make it challenging to extract the pure elastic scattering cross sections, with some authors instead presenting the vibrationally or electronically elastic cross sections. To our knowledge, only Linder and Schmidt [39] measured the rotationally elastic cross section. Ferch *et al.* [41], Furst *et al.* [42], Jones [43], and Subramanian and Kumar [44] measured the total cross section, which below around 10 eV is equivalent to the electronically elastic cross section. (The $b\,^3\Sigma_u^+$ excitation opens around 5 eV, but for $v_i = 0$ it makes an insignificant contribution to the total cross section below 10 eV [45].)

Our calculation of the rotationally elastic cross section falls within the error bars of Linder and Schmidt [39] but generally somewhat higher than the reported values, particularly at 0.3 eV. However, we note that at this energy the rotationally and electronically elastic cross sections are essentially the same, and our calculation of the latter is in good agreement with Ferch *et al.* [41] between 0.1 and 1.0 eV. Below 0.1 eV the measurements of Ferch *et al.* [41] are up to 20% larger than the MCCC calculations. At present we have no explanation for this except to say that we have verified convergence of the elastic cross section, and any potential uncertainties in the calculations due to numerical considerations cannot account for this discrepancy. Above 1 eV there is excellent agreement between the MCCC calculation of the electronically elastic cross section and the remaining measurements. A handful of measurements have been performed for the vibrationally elastic cross section, e.g., Brunger *et al.* [46] and references therein; however, we neglect them in Fig. 3 to maintain readability. We justify the omission by noting that the vibrationally and electronically elastic cross sections differ by only a few percent at most, there is already excellent agreement between MCCC and experiment for the latter, and the most recent vibrationally elastic measurements [46] come with error bars large enough to overlap the rotationally and electronically elastic cross sections. In Fig. 3 we compare the MCCC calculations and the measurements of Linder and Schmidt [39] for the rotationally elastic cross section with a number of previous calculations. The results of Morrison and Saha [26] and Trail *et al.* [34] are in good agreement with MCCC, while Morrison *et al.* [25] agrees with MCCC around 3 eV but is higher at lower energies, and Telega and Gianturco [24] is systematically 10%–15% higher than MCCC. The remaining calculations are in worse agreement with MCCC and predict different qualitative behavior of the cross section.

In Fig. 4 we present the momentum-transfer cross section

$$\sigma^{\rm mt} = \int \frac{d\sigma^{\rm elastic}}{d\Omega}(1-\cos\theta)d\Omega, \tag{29}$$

corresponding to each of the rotationally, vibrationally, and electronically elastic cross sections presented in Fig. 2. The difference between the three is smaller here than it is for the elastic scattering cross sections, but there is still a discrepancy of about 10% at the cross-section peak at around 2–3 eV, which will naturally impact the calculation of transport and rate coefficients. We compare with the swarm experiments of Crompton *et al.* [37], Gibson [38], and England *et al.* [28], which are in reasonable agreement with the vibrationally and electronically elastic MCCC momentum-transfer cross sections. Similarly to above, below 0.1 eV the MCCC cross section is somewhat lower than experiment, but here the discrepancy is at most 10%. We also include the cross section taken from the Biagi dataset on the LXCat database [47], which between 2 and 6 eV agrees with the MCCC

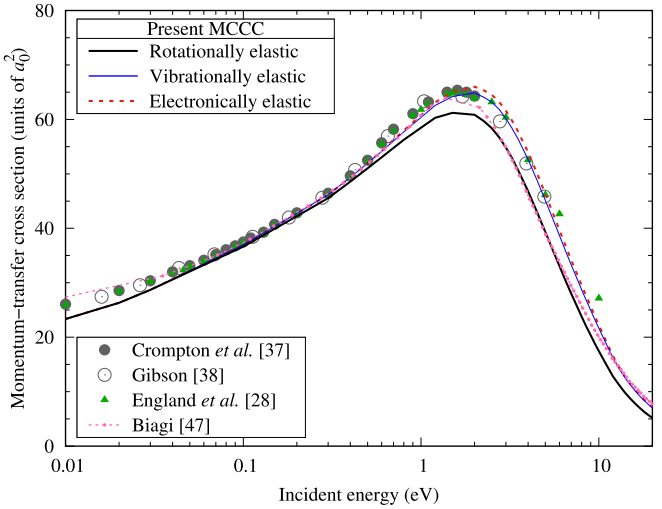

FIG. 4. Momentum-transfer cross sections for rotationally, vibrationally, and electronically elastic collisions with H_2. Comparison is made with the swarm experiments of Crompton *et al.* [37], Gibson [38], and England *et al.* [28], and data taken from the Biagi dataset on LXCat [47].

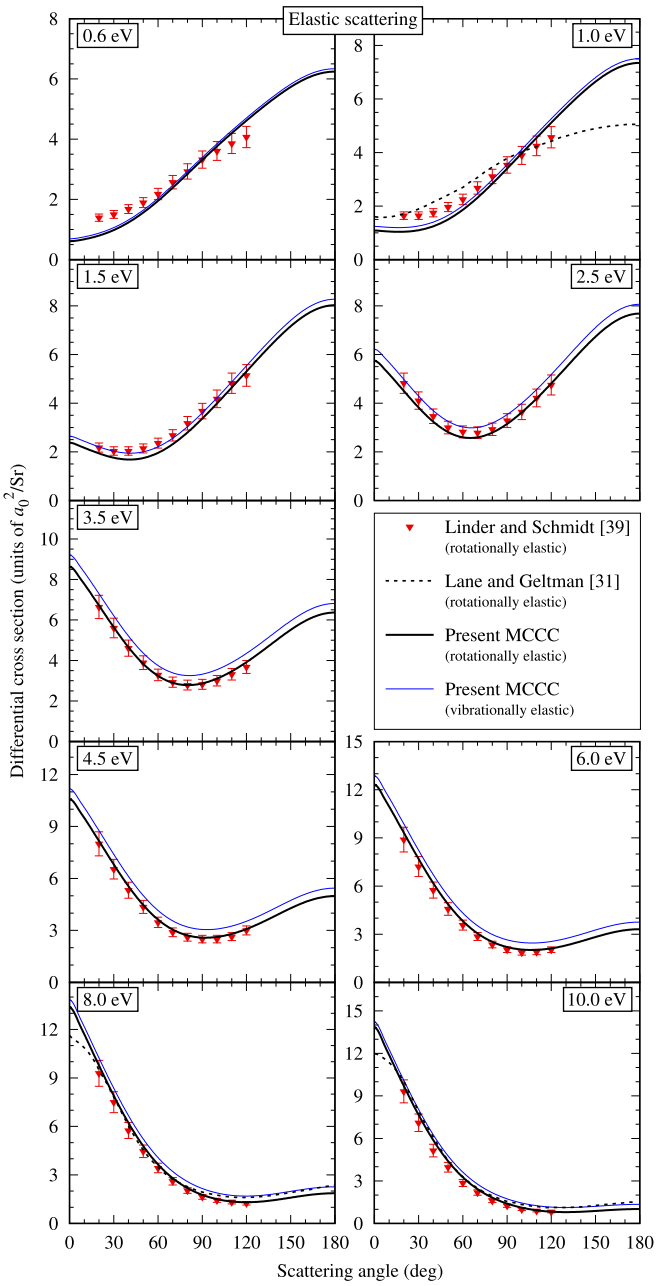

FIG. 5. Differential cross sections for rotationally and vibrationally elastic collisions with H_2. Comparison is made with the calculations of Lane and Geltman [31] and measurements of Linder and Schmidt [39].

rotationally elastic cross section and elsewhere agrees better with the electronically elastic cross section. Several of the authors referenced in Fig. 3 also calculated the momentum-transfer cross section, but since the comparison with MCCC is much the same as it is for the elastic scattering cross section, we exclude them from Fig. 4 to maintain readability. In Fig. 5 we present DCS for rotationally and vibrationally elastic scattering, and compare with the calculations of Lane and Geltman [31] and measurements of Linder and Schmidt [39] (both rotationally elastic). Within the AN approximation, the rotationally elastic cross section is independent of N_i, so the MCCC calculations presented here are for $N = 0 \rightarrow 0$, and they are directly comparable to the $N = 1 \rightarrow 1$ calculations of Lane and Geltman [31]. There is excellent agreement between the measurements and the MCCC calculations, aside from some slight discrepancies at the lower energies, and in several cases the experimental uncertainties are small enough that the measurements sit right on top of the MCCC rotationally elastic DCS without the error bars overlapping the vibrationally elastic DCS, a satisfying indication of the accuracy in the MCCC calculations. Note that we determined the uncertainty in the elastic DCS of Linder and Schmidt [39] to be 8.7% by combining (according to the Gauss error law) the three independent sources of 5% errors identified in points II, IV, and V of their discussion of errors. A detailed comparison of the MCCC electronically elastic DCS with various calculations and experiment can be found in the PhD thesis of Savage [20].

C. Rotational excitation

In Figs. 6 and 7 we present the $N = 0 \rightarrow 2$ (para-H_2) and $N = 1 \rightarrow 3$ (ortho-H_2) cross sections and compare with the large number of available calculations and measurements as cited in the figures. At low energies the MCCC calculations are in excellent agreement with the swarm measurements of Crompton *et al.* [37] and England *et al.* [28] for the $N = 0 \rightarrow 2$ transition and of England *et al.* [28] and Gibson [38] for $N = 1 \rightarrow 3$. Older swarm analysis was also performed by Engelhardt and Phelps [48]; however, their results are incompatible with the subsequent swarm studies cited above, so we do not present them here. There have been no beam measurements for the $N = 0 \rightarrow 2$ transition, so above 0.5 eV it is up to theory alone to determine the cross section. The greatest discrepancy between the various calculations is at the cross-section peak at around 4–5 eV. Being 100 times the threshold energy, one should expect the AN approximation to perform well here, and indeed, Morrison *et al.* [4] showed

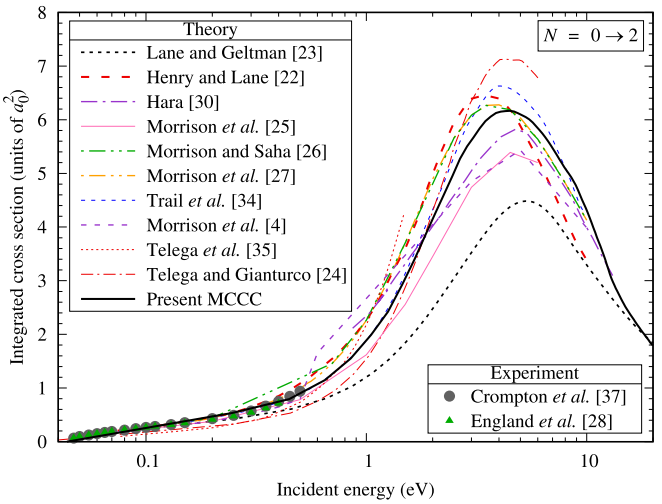

FIG. 6. Integrated cross section for the $N = 0 \rightarrow 2$ transition. Comparison is made with the calculations of Henry and Lane [22], Lane and Geltman [23], Morrison *et al.* [25], Morrison and Saha [26], Morrison *et al.* [27], Hara [30], Trail *et al.* [34], Telega *et al.* [35], Morrison *et al.* [4], and Telega and Gianturco [24], and the measurements of Crompton *et al.* [37] and England *et al.* [28].

this to be the case by comparing AN and RVCC calculations using identical potentials. Hence, we can only conclude that the differences between each of the calculations are due to the various choices of polarization and exchange potentials, and with the MCCC calculation being the only one with an exact account of exchange and coupling to closed electronic channels, we can have confidence in its validity.

For the $N = 1 \rightarrow 3$ transition there are beam measurements up to 10 eV from Ehrhardt and Linder [36], and Linder and Schmidt [39]. The MCCC cross section is in between the two sets of measurements but in better agreement with the

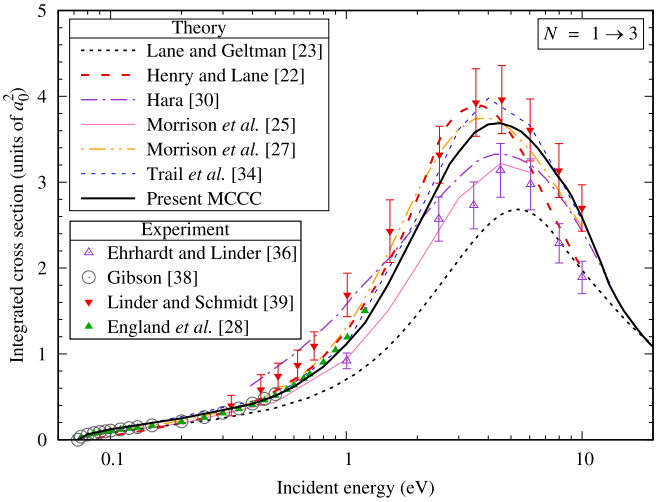

FIG. 7. Integrated cross section for the $N = 1 \rightarrow 3$ transition. Comparison is made with the calculations of Henry and Lane [22], Lane and Geltman [23], Hara [30], Morrison *et al.* [25,27], and Trail *et al.* [34], and the measurements of England *et al.* [28], Ehrhardt and Linder [36], Gibson [38], and Linder and Schmidt [39].

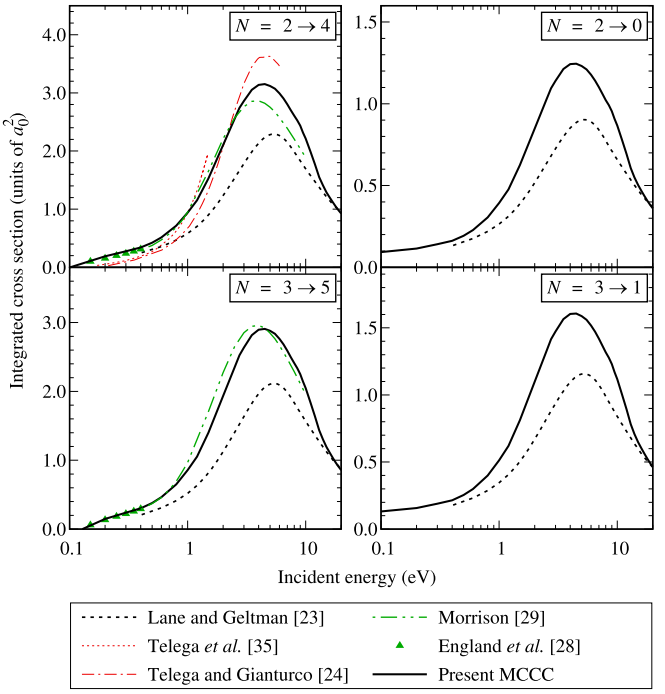

FIG. 8. Integrated cross section for the $N = 2 \rightarrow 4$, $2 \rightarrow 0$, $3 \rightarrow 5$, and $3 \rightarrow 1$ transitions. Comparison is made with the calculations of Lane and Geltman [23], Telega and Gianturco [24], Telega *et al.* [35], and Morrison [29], and the measurements of England *et al.* [28].

latter from 2 to 10 eV. From 0.4 to 2 eV our agreement with Linder and Schmidt [39] is worse, but the excellent agreement between MCCC and nearly all other theories and the swarm experiments at 0.4 eV suggests that Linder and Schmidt [39] have overestimated the cross section here. Here we have used an uncertainty of 10% for Linder and Schmidt [39], by combining the 8.7% uncertainty in the elastic DCS with the 5% uncertainty in the inelastic to elastic ratio specified in point I of their discussion of errors for energies 1.5 eV and above.

In Fig. 8 we present cross sections for the $N = 2 \rightarrow 4$, $2 \rightarrow 0$, $3 \rightarrow 5$, and $3 \rightarrow 1$ transitions, for which there are far fewer previous results to compare to. Lane and Geltman [23] calculated each of these cross sections, and the comparison with MCCC is the same for each as it was for the $N = 0 \rightarrow 2$ and $N = 1 \rightarrow 3$ transitions—perfect agreement at 20 eV but significant disagreement at lower energies due to their neglect of exchange. England *et al.* [28] provided swarm measurements of the $N = 2 \rightarrow 4$ and $3 \rightarrow 5$ cross sections, and as before they are in perfect agreement with MCCC. The calculations of Morrison [29] were provided to England *et al.* [28] as a private communication in order to extend the swarm cross sections above 0.4 eV, and hence we present them here as a calculation rather than experiment despite extracting them from England *et al.*'s [28] recommended cross section. The agreement between MCCC and Morrison [29] is good, aside from a small discrepancy around the peak of the $N = 2 \rightarrow 4$ cross section. The calculations of Telega *et al.* [35] and Telega and Gianturco [24] underestimate the $N = 2 \rightarrow 4$ cross section at low energies and overestimate around the peak.

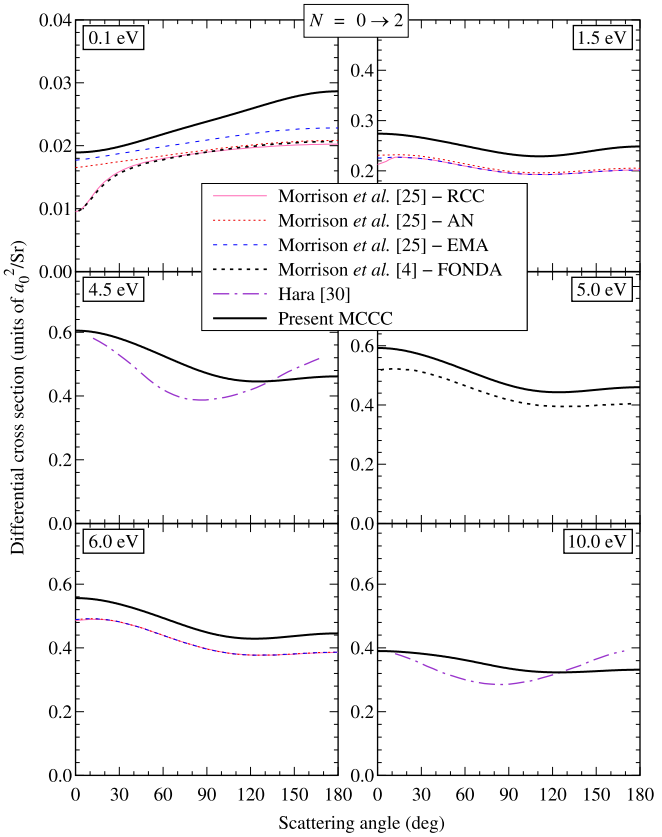

FIG. 9. Differential cross sections for the $N = 0 \rightarrow 2$ transition. Comparison is made with the calculations of Morrison *et al.* [25,4] using the RCC, AN, EMA, and FONDA techniques, and the AN calculation of Hara [30]. See Table II for acronym definitions.

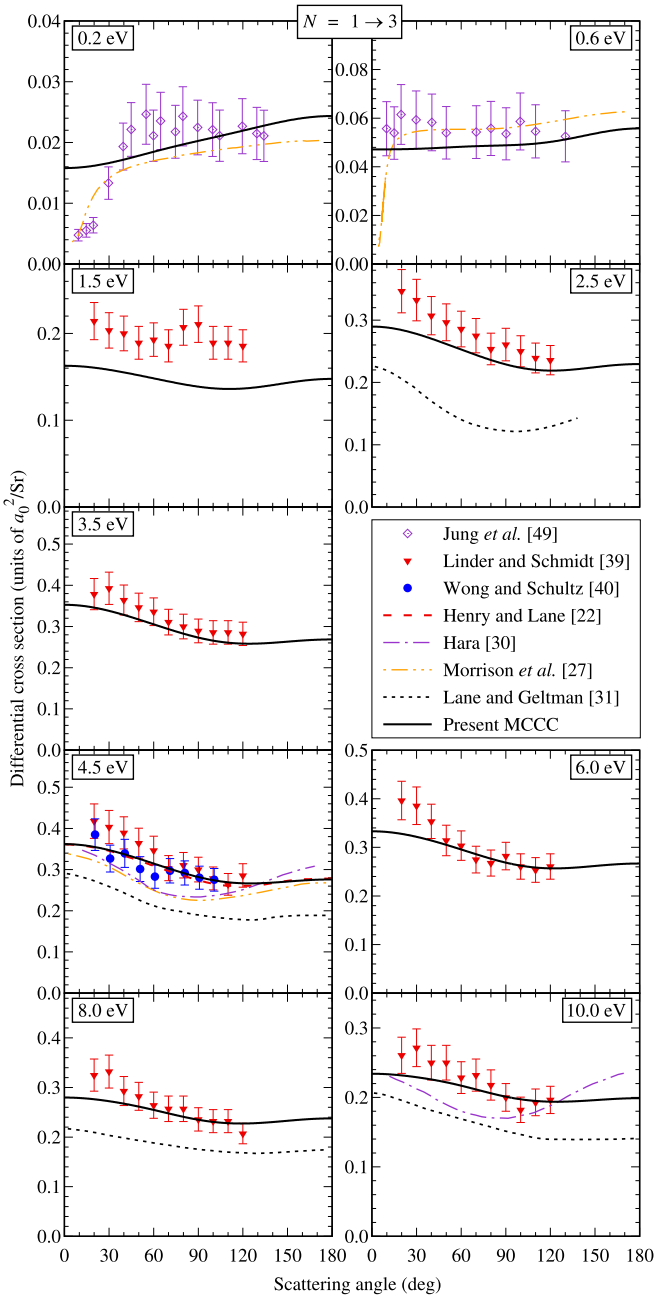

FIG. 10. Differential cross sections for the $N = 1 \rightarrow 3$ transition. Comparison is made with the calculations of Henry and Lane [22], Morrison *et al.* [27], Hara [30], and Lane and Geltman [31], and the measurements of Linder and Schmidt [39], Jung *et al.* [49], and Wong and Schultz [40].

In Fig. 9 we present DCS for the $N = 0 \rightarrow 2$ excitation, compared with the calculations of Morrison *et al.* [25,4] and Hara [30]. For the $N = 0 \rightarrow 2$ transition, Morrison *et al.* [25,4] compared their RVCC calculation (the most accurate treatment of the nuclear dynamics) with the AN approximation and the two modified adiabatic methods (EMA, FONDA) they proposed. At 0.1 eV there is a noticeable difference between the RVCC and AN DCS at forwards scattering angles. The AN approximation is typically applied with the additional assumption of degeneracy between the rovibrational energies, so that the same "on-shell" electronic scattering amplitudes can be used for all rovibrational transitions (on-shell here meaning that energy conservation is enforced at the level of the electronic scattering calculations but then violated in the AN calculations). The FONDA calculation of Morrison *et al.* [25] removes this degeneracy by using "off-shell" electronic amplitudes, and reproduces the RVCC DCS almost perfectly. Therefore, discrepancy between the AN and RCC DCS at 0.1 eV is not related to coupling between rotational levels but is rather a consequence of the violation of energy conservation in the standard AN approach. The MCCC calculations are qualitatively similar but systematically larger than Morrison *et al.* [25] at 0.1, 1.5, and 6.0 eV, in line with the underestimation of Morrison *et al.*'s [25] ICS for this transition seen in Fig. 6. The calculations of Hara [30] at 4.5 and 10.0 eV approach the same value as the MCCC DCS at forwards scattering, but they underestimate at 90 degrees and overestimate at backwards scattering.

In Fig. 10 we present DCS for the $N = 1 \rightarrow 3$ excitation, compared with the calculations of Henry and Lane [22], Morrison *et al.* [27], Hara [30], and Lane and Geltman [31], and the measurements of Linder and Schmidt [39], Jung *et al.* [49], and Wong and Schultz [40]. At 0.2 eV, the RVCC calculations of Morrison *et al.* [27] reproduce the forward-scattering angular dependence of the DCS measured by Jung *et al.* [49], while MCCC does not due to the breakdown of the AN

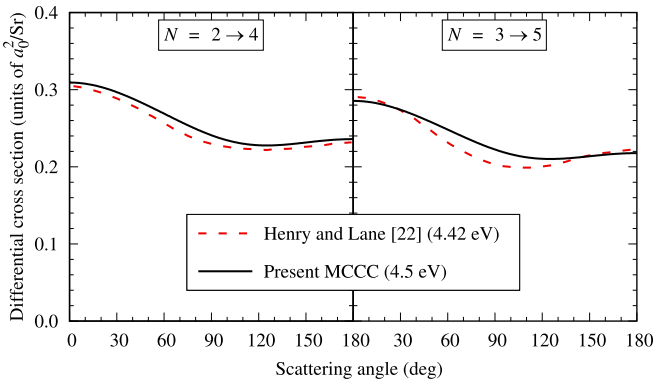

FIG. 11. Differential cross sections for the $N = 2 \rightarrow 4$ and $N = 3 \rightarrow 5$ transitions at 4.5 eV. Comparison is made with the calculations of Henry and Lane [22].

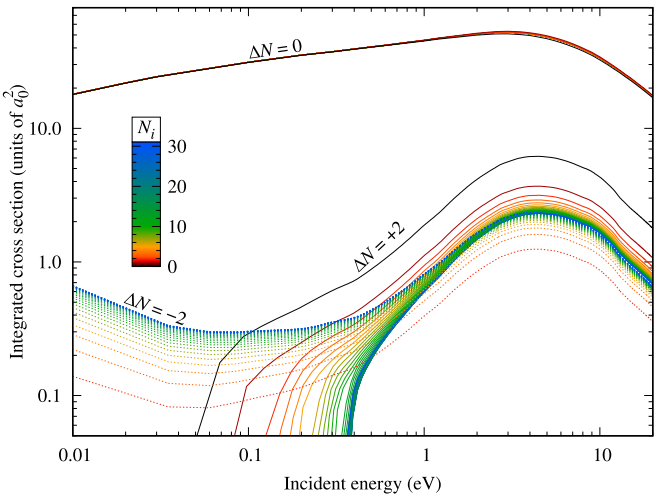

FIG. 12. Integrated cross sections for excitation ($\Delta N = 2$), deexcitation ($\Delta N = -2$), and elastic scattering ($\Delta N = 0$), illustrating the dependance on the initial rotational level N_i.

approximation at near-threshold energies. However, the magnitude of the MCCC DCS above 30 degrees is in somewhat better agreement with the experiment. At 0.6 eV the measurements agree better with Morrison *et al.* [27], though the error bars are large enough to overlap the MCCC DCS, and given that the MCCC ICS is in excellent agreement with the swarm measurements in this energy region (see Fig. 7), it is possible the beam measurements of Jung *et al.* [49] are somewhat too high. The agreement between MCCC and the Linder and Schmidt [39] DCS measurements follow what was seen in Fig. 7 for the ICS—worse at low energies and improving at higher energies, and again we suggest that the beam measurements may be too high at lower energies given the agreement between MCCC and the swarm experiments. At 4.5 eV and above, the Linder and Schmidt [39] and MCCC DCS are in good agreement between 60 and 120 degrees, with the MCCC result being lower than the measurements at smaller scattering angles. At 4.5 eV the calculation of Henry and Lane [22] is in perfect agreement with MCCC, and the measurements of Wong and Schultz [40] are in good agreement with MCCC (perfect above 60 degrees), being somewhat lower than Linder and Schmidt [39] below 70 degrees. Taking these facts into consideration, along with the excellent agreement between MCCC and Linder and Schmidt [39] for the rotationally elastic DCS, we suggest that the rotationally inelastic measurements of Linder and Schmidt [39] may be overestimated at smaller scattering angles and lower energies. The remaining previous calculations in Fig. 10 are all in poor agreement with MCCC and with experiment.

In Fig. 11 we present DCS for the $N = 2 \rightarrow 4$ and $3 \rightarrow 5$ excitations at 4.5 eV, compared with the calculations of Henry and Lane [22] (at 4.42 eV). There is good agreement between the two calculations. No other calculations or measurements have been performed for these transitions.

In Fig. 12 we present the entire set of cross sections with $|\Delta N| \leqslant 2$ and $N_i = 0$–31. The rotationally elastic cross sections are relatively insensitive to changes in N_i, while the excitation cross sections ($\Delta N = 2$) decrease with increasing N_i and vice versa for deexcitation ($\Delta N = -2$). The latter two have a similar energy dependence above 1 eV but deviate at lower energies, as the $\Delta N = 2$ transitions have thresholds not present in the $\Delta N = -2$ transitions. Around the peak of the cross sections it can be seen that the excitation and deexcitation cross sections both converge to a similar curve as N_i increases. This appears to be a result of the energy spacings between rotational levels becoming more regular as N increases, i.e., the energies fall more or less along a straight line for higher N as shown in Fig. 13, reducing the dependence of the inelastic cross sections on N_i.

V. CONCLUSIONS

We have performed calculations of elastic scattering and rotational excitation of H_2 by 0.01–20 eV electron impact using the adiabatic-nuclei molecular convergent close-coupling (MCCC) method. Integral and differential cross sections have been presented and compared with the available measurements and previous calculations. Agreement between the various theories is somewhat variable due to the use of model

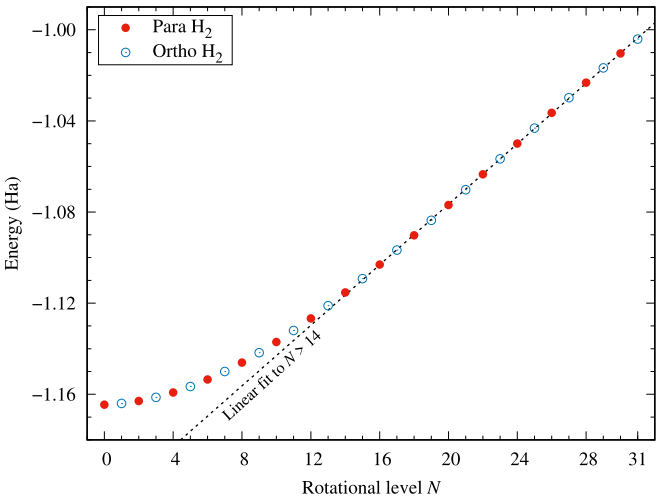

FIG. 13. Energies of the rotational levels in the $v = 0$ vibrational state of para- and ortho-H_2. A straight line is fitted to the $N > 14$ energies to indicate the more regular spacings between the higher levels.

polarization and exchange potentials in the previous calculations, which introduces significant error, while the present calculations solve the electronic component of the scattering problem without approximation. This source of uncertainty in the older calculations appears to be much more important than the differences between the various approaches to modeling the nuclear dynamics, which is what much of the previous work has focused on.

Agreement between the present calculations and integral cross sections derived from swarm experiments is excellent where they are available, while agreement with beam experiments is poorer at low energies. Above 4 eV we find overall good agreement with the integral and differential cross sections from the beam measurements, but suggest that Linder and Schmidt [39] may have overestimated the cross section at scattering angles below 60 degrees. A measurement of the 4.5 eV $N = 1 \rightarrow 3$ differential cross section by Wong and Schultz [40] supports this assertion.

Some of the present cross sections have already been utilized in a study of the cosmic-ray ionization rate in molecular clouds [2], and we expect that they will be useful for future modeling of low-temperature plasmas such as those found in astrophysical environments or the edge, divertor, and ion-source plasmas in fusion research. The results presented here can be downloaded from the MCCC database [13].

ACKNOWLEDGMENTS

This research was supported by the Australian Government through the Australian Research Council's *Discovery Projects* funding scheme (Project No. DP190101195), and by the United States Air Force Office of Scientific Research. HPC resources were provided by the Pawsey Supercomputing Research Centre with funding from the Australian Government and the Government of Western Australia, and the Texas Advanced Computing Center (TACC) at The University of Texas at Austin. We also acknowledge the support of the Australasian Leadership Computing Grants scheme, with computational resources provided by NCI Australia, an NCRIS-enabled capability supported by the Australian Government. M.C.Z. would like to specifically acknowledge the support of the Los Alamos National Laboratory (LANL) ASC PEM Atomic Physics Project. LANL is operated by Triad National Security LLC for the National Nuclear Security Administration of the U.S. Department of Energy under Contract No. 89233218NCA000001.

[1] J.-S. Yoon, M.-Y. Song, J.-M. Han, S. H. Hwang, W.-S. Chang, B. Lee, and Y. Itikawa, J. Phys. Chem. Ref. Data **37**, 913 (2008).
[2] M. Padovani, S. Bialy, D. Galli, A. V. Ivlev, T. Grassi, L. H. Scarlett, U. S. Rehill, M. C. Zammit, D. V. Fursa, and I. Bray, Astron. Astrophys. **658**, A189 (2022).
[3] K. Sawada and M. Goto, Atoms **4**, 29 (2016).
[4] M. A. Morrison, M. Abdolsalami, and B. K. Elza, Phys. Rev. A **43**, 3440 (1991).
[5] M. C. Zammit, J. S. Savage, D. V. Fursa, and I. Bray, Phys. Rev. Lett. **116**, 233201 (2016).
[6] M. C. Zammit, J. S. Savage, D. V. Fursa, and I. Bray, Phys. Rev. A **95**, 022708 (2017).
[7] L. H. Scarlett, D. V. Fursa, M. C. Zammit, I. Bray, Yu. Ralchenko, and K. D. Davie, At. Data Nucl. Data Tables **137**, 101361 (2021).
[8] L. H. Scarlett, D. V. Fursa, M. C. Zammit, I. Bray, Yu. Ralchenko, and K. D. Davie, At. Data Nucl. Data Tables **139**, 101403 (2021).
[9] L. H. Scarlett, D. K. Boyle, M. C. Zammit, Yu. Ralchenko, I. Bray, and D. V. Fursa, At. Data Nucl. Data Tables **148**, 101534 (2022).
[10] L. H. Scarlett, E. Jong, S. Odelia, M. C. Zammit, Yu. Ralchenko, B. I. Schneider, I. Bray, and D. V. Fursa, At. Data Nucl. Data Tables **151**, 101573 (2023).
[11] D. Wünderlich, L. H. Scarlett, S. Briefi, U. Fantz, M. C. Zammit, D. V. Fursa, and I. Bray, J. Phys. D: Appl. Phys. **54**, 115201 (2021).
[12] L. H. Scarlett, U. S. Rehill, M. C. Zammit, K. Bartschat, I. Bray, and D. V. Fursa, Phys. Rev. A **104**, L040801 (2021).
[13] mccc-db.org
[14] L. H. Scarlett, Ph.D. thesis, Curtin University, 2021.
[15] J. Brown and A. Carrington, *Rotational Spectroscopy of Diatomic Molecules* (Cambridge University Press, Cambridge, 2003).
[16] L. H. Scarlett, J. S. Savage, D. V. Fursa, I. Bray, M. C. Zammit, and B. I. Schneider, Phys. Rev. A **103**, 032802 (2021).
[17] J.-L. Meunier, Eur. J. Phys. **8**, 114 (1987).
[18] L. H. Scarlett, I. Bray, and D. V. Fursa, Phys. Rev. Lett. **127**, 223401 (2021).
[19] M. C. Zammit, D. V. Fursa, J. S. Savage, and I. Bray, J. Phys. B: At. Mol. Opt. Phys. **50**, 123001 (2017).
[20] J. S. Savage, Ph.D. thesis, Curtin University, 2018.
[21] H. S. W. Massey and R. O. Ridley, Proc. Phys. Soc. Sect. A **69**, 659 (1956).
[22] R. J. W. Henry and N. F. Lane, Phys. Rev. **183**, 221 (1969).
[23] N. F. Lane and S. Geltman, Phys. Rev. **160**, 53 (1967).
[24] S. Telega and F. A. Gianturco, Eur. Phys. J. D **36**, 271 (2005).
[25] M. A. Morrison, A. N. Feldt, and D. Austin, Phys. Rev. A **29**, 2518 (1984).
[26] M. A. Morrison and B. C. Saha, Phys. Rev. A **34**, 2786 (1986).
[27] M. A. Morrison, R. W. Crompton, B. C. Saha, and Z. Lj. Petrović, Aust. J. Phys. **40**, 239 (1987).
[28] J. P. England, M. T. Elford, and R. W. Crompton, Aust. J. Phys. **41**, 573 (1988).
[29] M. A. Morrison, Private communication in Ref. [28], 1986.
[30] S. Hara, J. Phys. Soc. Jpn. **27**, 1592 (1969).
[31] N. F. Lane and S. Geltman, Phys. Rev. **184**, 46 (1969).
[32] R. J. W. Henry, Phys. Rev. A **2**, 1349 (1970).
[33] R. J. W. Henry and E. S. Chang, Phys. Rev. A **5**, 276 (1972).
[34] W. K. Trail, M. A. Morrison, W. A. Isaacs, and B. C. Saha, Phys. Rev. A **41**, 4868 (1990).
[35] S. Telega, E. Bodo, and F. A. Gianturco, Eur. Phys. J. D **29**, 357 (2004).

[36] H. Ehrhardt and F. Linder, Phys. Rev. Lett. **21**, 419 (1968).
[37] R. W. Crompton, D. K. Gibson, and A. I. McIntosh, Aust. J. Phys. **22**, 715 (1969).
[38] D. K. Gibson, Aust. J. Phys. **23**, 683 (1970).
[39] F. Linder and H. Schmidt, Z. Naturforsch. A **26**, 1603 (1971).
[40] S. F. Wong and G. J. Schultz, Phys. Rev. Lett. **32**, 1089 (1974).
[41] J. Ferch, W. Raith, and K. Schröder, J. Phys. B: At. Mol. Phys. **13**, 1481 (1980).
[42] J. Furst, M. Mahgerefteh, and D. E. Golden, Phys. Rev. A **30**, 2256 (1984).
[43] R. K. Jones, Phys. Rev. A **31**, 2898 (1985).
[44] K. P. Subramanian and V. Kumar, J. Phys. B: At. Mol. Opt. Phys. **22**, 2387 (1989).
[45] L. H. Scarlett, D. V. Fursa, J. Knol, M. C. Zammit, and I. Bray, Phys. Rev. A **103**, L020801 (2021).
[46] M. J. Brunger, S. J. Buckman, D. S. Newman, and D. T. Alle, J. Phys. B: At. Mol. Opt. Phys. **24**, 1435 (1991).
[47] Biagi database, lxcat.net/Biagi, retrieved March 7, 2023.
[48] A. G. Engelhardt and A. V. Phelps, Phys. Rev. **131**, 2115 (1963).
[49] K. Jung, K.-M. Scheuerlein, W. Sohn, K.-H. Kochem, and H. Ehrhardt, J. Phys. B: Atom. Mol. Phys. **20**, L327 (1987).